AGU PUBLICATIONS

JGR

Journal of Geophysical Research: Oceans

RESEARCH ARTICLE

10.1002/2016JC011852

**Key Points:**
- Air-sea gas exchange parameterizations are evaluated
- Air-sea gas transfer for flows driven by natural convection and wind
- Transition by gas transfer dominated of natural convection versus wind

**Correspondence to:**
S. T. Fredriksson,
sam.fredriksson@gu.se

**Citation:**
Fredriksson, S. T., L. Arneborg, H. Nilsson, and R. A. Handler (2016), Surface shear stress dependence of gas transfer velocity parameterizations using DNS, *J. Geophys. Res. Oceans*, *121*, 7369–7389, doi:10.1002/2016JC011852.

Received 31 MAR 2016
Accepted 11 SEP 2016
Accepted article online 15 SEP 2016
Published online 8 OCT 2016



# Surface shear stress dependence of gas transfer velocity parameterizations using DNS

**S. T. Fredriksson[1], L. Arneborg[1,2], H. Nilsson[3], and R. A. Handler[4]**

[1]Department of Marine Sciences, University of Gothenburg, Gothenburg, Sweden, [2]Department of Research and Development, Swedish Meteorological and Hydrological Institute, Västra Frölunda, Sweden, [3]Department of Applied Mechanics, Fluid Dynamics, Chalmers University of Technology, Gothenburg, Sweden, [4]Department of Mechanical Engineering, Texas A&M University, College Station, Texas, USA

**Abstract** Air-water gas-exchange is studied in direct numerical simulations (DNS) of free-surface flows driven by natural convection and weak winds. The wind is modeled as a constant surface-shear-stress and the gas-transfer is modeled via a passive scalar. The simulations are characterized via a Richardson number $Ri=Bv/u_*^4$ where $B$, $v$, and $u_*$ are the buoyancy flux, kinematic viscosity, and friction velocity respectively. The simulations comprise $0 < Ri < \infty$ ranging from convection-dominated to shear-dominated cases. The results are used to: (i) evaluate parameterizations of the air-water gas-exchange, (ii) determine, for a given buoyancy flux, the wind speed at which gas transfer becomes primarily shear driven, and (iii) find an expression for the gas-transfer velocity for flows driven by both convection and shear. The evaluated gas transfer-velocity parametrizations are based on either the rate of turbulent kinetic energy dissipation, the surface flow-divergence, the surface heat-flux, or the wind-speed. The parametrizations based on dissipation or divergence show an unfavorable $Ri$ dependence for flows with combined forcing whereas the parametrization based on heat-flux only shows a limited $Ri$ dependence. The two parametrizations based on wind speed give reasonable estimates for the transfer-velocity, depending however on the surface heat-flux. The transition from convection- to shear-dominated gas-transfer-velocity is shown to be at $Ri \approx 0.004$. Furthermore, the gas-transfer is shown to be well represented by two different approaches: (i) additive forcing expressed as $k_{g,sum}=A_{Shear}u_*(Ri/Ri_c+1)^{1/4}Sc^{-n}$ where $Ri_c=\left(A_{Shear}/A_{Buoy}\right)^4$, and (ii) either buoyancy or shear dominated expressed as, $k_g=A_{Buoy}(Bv)^{1/4}Sc^{-n}$, $Ri > Ri_c$ or $k_g=A_{shear}u_*Sc^{-n}$, $Ri < Ri_c$. Here $A_{Buoy}=0.4$ and $A_{Shear}=0.1$ are constants, and $n$ is an exponent that depends on the water surface-characteristics.

## 1. Introduction

"There is little doubt that the neutral pipe hypothesis [meaning that gas-exchange in freshwater is negligible] is untenable, and that freshwater ecosystems represent an active component of the global carbon cycle that deserve attention." [*Cole et al.*, 2007]. These freshwater ecosystems (rivers, streams and lakes) are in recent global-model estimates found to be sources of atmospheric greenhouse gases of the same magnitude as the ocean net sink [*Ciais et al.*, 2013]. This increased interest in air-water gas exchange in low-wind environments, as freshwater systems often are, is the main motivation for this work. This work is a continuation of the work presented by *Fredriksson et al.* [2016]. It is naturally relevant for the gas flux in the ocean during low wind conditions as well.

Direct numerical simulations (DNS) and large eddy simulations (LES) have been used with success to study the air-sea gas exchange dependence on the rate of turbulent kinetic energy dissipation via a turbulent Reynolds number $Re_T$ [*Calmet and Magnaudet*, 1998] and as a function of the horizontal flow divergence [*Banerjee et al.*, 2004; *Calmet and Magnaudet*, 1998; *Magnaudet and Calmet*, 2006]. In addition, the Schmidt number dependency on the gas transfer velocity [*Hasegawa and Kasagi*, 2008; *Herlina and Wissink*, 2014; *Kubrak et al.*, 2013; *Na et al.*, 1999; *Nagaosa and Handler*, 2012; *Nagaosa*, 2014; *Wissink and Herlina*, 2016] and the influence of surfactants on the gas exchange [*Hasegawa and Kasagi*, 2008; *Zhang et al.*, 2013] have been studied. Beside the numerical approach many field studies have been performed in order to estimate the gas exchange [e.g., *Gålfalk et al.*, 2013; *Rantakari et al.*, 2015].

*Fredriksson et al.* [2016] performed DNS for turbulent flow driven by pure natural convection in order to understand which processes control the gas transfer velocity. The second objective was to evaluate

different methods of parameterizing the gas transfer velocity. Furthermore, the appropriate mesh resolution and domain aspect-ratio were found via an extensive mesh resolution and domain aspect-ratio sensibility study. It was found that the gas transfer velocity could be expressed by $k_s = A\ (Bv)^{1/4}\ Sc^{-n}$, where $A$ is a constant, $B$ is the buoyancy flux, $v$ is the kinematic viscosity, $Sc = v/D$ is the Schmidt number, $D$ is the molecular diffusivity, and the exponent $n$ depends on the characteristics of the water surface (i.e., abundance of surfactant). The results suggested that $A = 0.39$ and that $n \approx 1/2$ for slip and $n \approx 2/3$ for no-slip boundary conditions at the surface, respectively. These boundary conditions were found to resemble a clean surface and a surface with a large abundance of surfactants (saturated conditions). All the evaluated parameterizations including two standard wind parameterizations, as well as parameterizations in terms of the rate of turbulent kinetic energy dissipation, the surface flow divergence, and the surface heat flux gave reasonable results. However, one wind parameterization overestimated and the other underestimated the gas transfer velocity compared to the DNS results. The present paper follows the same structure as *Fredriksson et al*. [2016]. All necessary equations are given in both papers but the background and origin of the equations are more thoroughly given by *Fredriksson et al*. [2016]. They also give a more thorough literature review.

The main objective of the present work is to extend the work by *Fredriksson et al*. [2016] in order to quantify the interaction between buoyancy flux and wind shear-stress, and how this interaction influences air-water gas exchange and, more specifically, the gas transfer velocity. The second objective is to evaluate different gas-transfer-velocity parameterizations for three different low-wind flow conditions which are relevant for small sheltered lakes and low wind conditions in the ocean. These conditions comprise natural convection only, wind shear stress only and finally a combination of these. The evaluated parameterizations include two standard wind parameterizations, as well as parameterizations in terms of the rate of turbulent kinetic energy dissipation, the surface flow divergence, and the surface heat flux. The evaluation is performed via highly resolved DNS. This is, to the best knowledge of the authors, the first time these gas transfer velocity parameterizations have been evaluated altogether using DNS for flows driven by both natural convection and surface shear stress, thus enabling a systematic and consistent comparison of the parameterizations.

### 1.1. Gas Transfer Parameterizations

Emissions of diffusive $CO_2$ and $CH_4$ from aquatic ecosystems are generally estimated using

$$F = k_g(c_w - \vartheta c_a), \tag{1}$$

where $F$ is a water-side controlled gas flux, $k_g$ is the gas transfer velocity, $c_w$ and $c_a$ are the gas concentrations in the surface water under the diffusive sublayer and in the air respectively and $\vartheta$ is the dimensionless Ostwald solubility coefficient of the gas in water. Note that ebullition must be added in order to get the total emission of $CH_4$. The most common method to estimate $k_g$ is through a parameterization via the wind speed 10 meters above the surface, referred to as $U_{10}$. The two parameterizations studied here are given by *Cole and Caraco* [1998] as

$$k_{g,CC1998,600} = 0.215U_{10}^{1.7} + 2.07 \tag{2}$$

often used for inland waters and *Wanninkhof et al*. [2009] as

$$k_{g,W2009,660} = 0.1U_{10} + 0.064U_{10}^2 + 0.011U_{10}^3 + 3 \tag{3}$$

often used for the oceans. Equations (2) and (3) are derived empirically and must be used with the associated units, i.e. $U_{10}[m\ s^{-1}]$ and $k_g[cm\ h^{-1}]$ since they are dimensionally inconsistent. Furthermore, they are given for gases with Schmidt number $Sc = 600$ and $Sc = 660$ representing $CO_2$ in fresh and salt water, respectively. The relation between two transfer velocities with different gas-water properties are generally expressed via their different $Sc$ numbers as

$$k_{g,Sc_1} = k_{g,Sc_2}\left(\frac{Sc_1}{Sc_2}\right)^{-n}. \tag{4}$$

The exponent, $n$, depends on the water surface characteristics and should be in the range of $1/2 < n < 2/3$. It was confirmed by *Fredriksson et al*. [2016] to be approximately $1/2$ for a clean surface modeled with a slip condition, and $2/3$ for a surface with saturated surfactant conditions modeled with a no-slip surface boundary conditions. We don't expect $n$ to be different in the present case and therefore only investigate clean surfaces (with a slip condition).

The following parameterizations, using either the rate of turbulent kinetic energy dissipation, $\varepsilon$, the surface flow divergence, $\gamma_{rms}$, or the heat transfer velocity, $\kappa_{heat}$, are derived theoretically. These contain, however, nondimensional constants that need to be determined numerically or empirically. The parameterization using the turbulent kinetic energy dissipation, $\varepsilon$, defined and discussed in section 3.1, is given by

$$k_{g,diss}=A_{diss}(\varepsilon\nu)^{1/4}Sc^{-n}, \tag{5}$$

where $A_{diss}$ is a transfer velocity constant. The parameterization using the horizontal flow divergence at the surface is given by

$$k_{g,div}=A_{div}(\gamma_{rms}\nu)^{1/2}Sc^{-n}, \tag{6}$$

where $\gamma_{rms}$ is the root-mean-square (RMS) of the surface flow divergence, defined and discussed in section 3.3.2, and $A_{div}$ is a transfer velocity constant. The parameterization using heat flux uses the heat transfer velocity, $\kappa_{heat}$, as

$$k_{g,heat}=A_{heat}\kappa_{heat}\left[\frac{Sc}{Pr}\right]^{-n},\quad \kappa_{heat}=\frac{Q_0}{\rho c_p\Delta T}. \tag{7}$$

Here $Pr=\nu/\alpha$ is the Prandtl number, $\alpha$ is the thermal diffusivity, and $A_{heat}$ is a transfer velocity constant. In addition, $Q_0$ is the vertical heat flux at the air-water interface due to latent and sensible heat fluxes as well as longwave radiation, $\Delta T$ is the surface skin-bulk temperature difference across the thermal boundary layer, $\rho$ is the density, and $c_p$ is the specific heat capacity. *Fredriksson et al.* [2016] found the constants to be $A_{diss}=0.45$, $A_{div}=0.57$, and $A_{heat}=0.90$ for pure natural convection. $CO_2$ and $CH_4$ are in the present DNS study treated as inert gases [*Broecker and Peng*, 1974].

### 1.2. Scaling

In the present study we investigate the functional relationships $\psi$ between the gas transfer velocity and the dependent variables for cases in which the fluid forcing is due to (I) pure natural convection where $k_g=\psi_I(D,\nu,\alpha,B,H)$, (II) surface shear stress where $k_g=\psi_{II}(D,\nu,u_*,H)$, and (III) a combination of natural convection and surface shear-stress where $k_g=\psi_{III}(D,\nu,\alpha,B,u_*,H)$. Here $\alpha$ is the thermal diffusivity, $B=\beta g Q_0/\rho c_p$ is the buoyancy flux just below the surface where $\beta$ is the coefficient of thermal expansion, $g$ is the gravitational acceleration, $u_*=(\tau_0/\rho)^{1/2}$ is the friction velocity where $\tau_0$ is the surface shear stress, and $H$ is the surface mixed-layer thickness. A dimensional analysis of these three cases leads to the nondimensional relations $\varphi_I-\varphi_{III}$ for the gas transfer velocity as:

$$\frac{k_g}{(B\nu)^{1/4}}=\varphi_I(Sc,Pr,Ra) \tag{8}$$

for natural convection,

$$\frac{k_g}{u_*}=\varphi_{II}(Sc,Re_*) \tag{9}$$

for surface shear stress, and

$$\frac{k_g}{u_*}=\varphi_{III}(Sc,Pr,Re_*,Ri) \tag{10}$$

for the combined case. In the above equations,

$$Ra=\frac{BH^4}{\alpha^2\nu} \tag{11}$$

is the Rayleigh number,

$$Re_*=\frac{u_*H}{\nu}, \tag{12}$$

is the surface shear-based Reynolds number, and

$$Ri = \frac{Bv}{(u_*)^4} \left( = \frac{Ra}{Pr^2 Re_*^4} \right) \tag{13}$$

is a Richardson number.

Equation (8) was confirmed by *Fredriksson et al.* [2016] to be well described with $k_g \propto Sc^{-n}(Bv)^{1/4}$ for large enough *Ra* numbers and for a constant *Pr* number.

There are many other alternatives to equation (10), e.g., one could use the Rayleigh number instead of the Richardson number, but since the Richardson number expresses the relative importance of buoyancy and shear forcing, it is in the present study used to define the transition between the two types of forcing.

Here, as discussed by *Fredriksson et al.* [2016], inner scaling denoted $\langle\ \rangle^+$ is used for diffuse boundary layer phenomena and outer scaling denoted $\langle\ \rangle^*$ is used for mixed-layer phenomena. The time scales, $t^+ = L^+/W^+ = Sc^{2n-1}(B/v)^{-1/2}$ and $t^* = L_z/W^* = \left(B/L_z^2\right)^{-1/3}$ are appropriate for natural convection. $L_z = H$ is assumed to represent the mixed-layer thickness in equations (11) and (12).

For a shear driven flow, the typical velocity and length scales are the friction velocity $u_*$ and $L_* = v/u_*$. It can be noted that this shear length-scale ($L_*$) is frequently used in the fluid-mechanics literature to define the nondimensional distance from the wall $y^+ = z/L_*$. In the figures in the present study, however, $z/L_*$ will be used instead of $y^+$ in order to minimize the risk of misinterpretations between $y^+$ and the inner scales driven by convection. The corresponding time scales for shear driven flows are $t_{*,inner} = v/u_*^2$ and $t_{*,outer} = L_z/u_*$.

## 2. Problem Formulation and Numerical Method

A passive scalar is used to model the transport of a dissolved inert gas in a DNS of a fully developed turbulent flow driven by natural convection and/or surface shear stress. The gas transfer-velocity parameterizations are evaluated by comparing them to the scalar transfer velocity

$$k_{s,Sc} = \frac{F_{s0,Sc}}{\Delta s_{Sc}} \tag{14}$$

where $F_{s_0,Sc}$ is the mean scalar flux across the surface for a scalar with a Schmidt number *Sc*. $\Delta s_{Sc}$ is the scalar-concentration difference across the diffusive boundary layer. The gas transfer-velocity parameterizations in equations (2)–(7) are studied by evaluating $\varepsilon, \gamma, Q_0/\Delta T$, and $k_{s,Sc}$. The rectangular computational domain is shown in Figure 1 where the streamwise, spanwise and surface-normal directions are denoted *x*, *y*, and *z* respectively. The surface boundary is located at $z = 0$ and the bottom boundary at $z = -L_z$. The lateral dimensions are $L_x = 3\pi L_z$ and $L_y = \pi L_z$ respectively. A summary of the parameters used in each simulation is given in Table 1. The first case, although originally presented by *Fredriksson et al.* [2016], is given for completeness since it will be discussed in the results and section 3. The cases are labeled with a number for $Re_*$ and *B* or *NB* describing whether there is buoyancy forcing (*B*) or no buoyancy forcing (*NB*). In the no buoyancy cases (the cases in which there is no natural convection) the temperature field acts as a passive scalar.

### 2.1. Mathematical Formulation

The equations to be solved are the incompressible Navier-Stokes equations

$$\frac{\partial \mathbf{U}}{\partial t} + \mathbf{U} \cdot \nabla\ \mathbf{U} = \mathbf{f} - \frac{1}{\rho_0}\nabla P + v\nabla^2\mathbf{U} + \beta g\ (T - T_0)\mathbf{k} \tag{15}$$

$$\nabla \mathbf{U} = 0 \tag{16}$$

where the standard Boussinesq approximation has been used, the thermal energy equation

$$\frac{\partial T}{\partial t} + \mathbf{U} \cdot \nabla\ T = \alpha\nabla^2 T + \phi_T, \tag{17}$$

and the transport equation for the passive scalar

$$\frac{\partial S}{\partial t} + \mathbf{U} \cdot \nabla\ S = D\nabla^2 S + \phi_s, \tag{18}$$

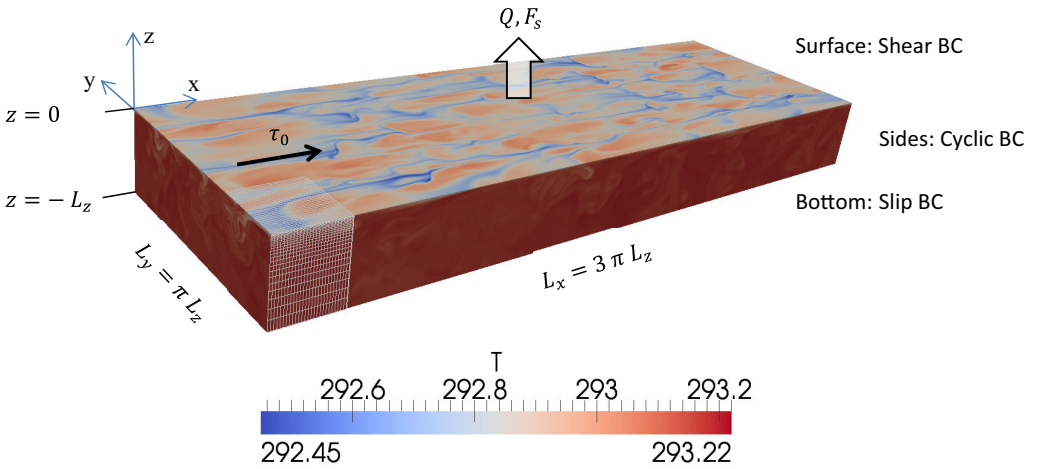


**Figure 1.** Computational domain with the temperature field for 240*NB*. The domain size is given by $L_z$, $L_x = 3\pi L_z$ and $L_y = \pi L_z$ in the depth, streamwise, and spanwise direction respectively. The surface is subject to a constant outward going heat flux, $Q_0$, and a constant scalar concentration, $F_{s0}$, while the bottom is subject to an insulation and a zero scalar-flux boundary conditions. The velocity boundary conditions are either slip or constant shear stress, $\tau_0$, at the surface boundary and slip at the bottom boundary.

which is used to model dissolved gases. Here the equations are presented in dimensional form following *Fredriksson et al*. [2016] in order to be able to apply different normalization at the results. $\mathbf{U} = (U, V, W)$ is the fluid velocity and $t$ is time. $\mathbf{f}$ is a pressure gradient in the $x$-direction only, balancing the applied surface shear stress in order to prevent the mean flow from accelerating. The background hydrostatic pressure for a constant density is subtracted and is included in the modified pressure $P$, $\nu$ is the kinematic viscosity, $\mathbf{k}$ is a unit vector in the vertical direction, and $g$ is the gravitational acceleration (equal to zero in the *NB* cases). The density $\rho$ is assumed to be a linear function of the temperature $T$ where $\beta = -\frac{1}{\rho_0}\frac{\partial \rho}{\partial T}\big|_0$ is the coefficient of thermal expansion, $\rho_0$ is the reference density, and $T_0$ is a reference fluid temperature. $\phi_T$ and $\phi_s = F_{s0}/L_z$ are spatially and temporally constant source terms added to maintain a constant mean temperature and a constant mean scalar flux $F_{s0}$ through the surface boundary, respectively. The mean scalar flux $F_{s0}$ is used in equation (14) to calculate the scalar transfer velocity.

The surface boundary is assumed to be flat, meaning that the surface deflection is negligible. The surface velocity boundary conditions are given in Table 1. The $x$-component of the velocity is given a constant shear-stress condition $\mu \partial U/\partial z = \tau_0$ at the surface where $\mu$ is the dynamic viscosity. This can be written as $\partial U/\partial z = \nu (Re_*/L_z)^2$ (Table 1). The boundary conditions in the $y$ (spanwise) and $z$ (surface-normal) directions are $\partial V/\partial z = W = 0$ at the surface. The bottom boundary is assumed to be stress-free and is thus given a slip boundary condition via $\partial U/\partial z = \partial V/\partial z = W = 0$.

During natural convection conditions with no or low wind, the surface heat flux is dominated by long-wave radiation and latent heat flux, both assumed to be constant in the simulations. This allows the use of a

**Table 1.** Summary of Numerical Cases[a]

| Case[b] | $u_*$ ($mms^{-1}$) | $U_{10}$ ($ms^{-1}$]) | $Ri \cdot 10^{-3}$ | $L_x, L_y$ | No. cells x,y,z | Surface BC[c] $\partial U/\partial z, \partial V/\partial z,$ | g ($ms^{-2}$) |
|---|---|---|---|---|---|---|---|
| 0*B* | | | | $2L_z$ | 256, 256, 96 | 0, 0 | 9.81 |
| 120*B* | 1.0 | 0.86 | 49.3 | $3\pi L_z, \pi L_z$ | 1206, 402, 96 | $\nu(120/L_z)^2$, 0 | 9.81 |
| 120*NB* | 1.0 | 0.86 | | $3\pi L_z, \pi L_z$ | 1206, 402, 96 | $\nu(120/L_z)^2$, 0 | |
| 180*B* | 1.5 | 1.33 | 9.74 | $3\pi L_z, \pi L_z$ | 1206, 402, 96 | $\nu(180/L_z)^2$, 0 | 9.81 |
| 180*NB* | 1.5 | 1.33 | | $3\pi L_z, \pi L_z$ | 1206, 402, 96 | $\nu(180/L_z)^2$, 0 | |
| 240*B* | 2.0 | 1.81 | 3.08 | $3\pi L_z, \pi L_z$ | 1206, 402, 96 | $\nu(240/L_z)^2$, 0 | 9.81 |

[a] $U_{10}$, $Ri$, and $Ra = 5.0 \cdot 10^8$ are calculated for a water and air temperature of 20°*C* with $Q_0 = 100$ $Wm^{-2}$ and $L_z = 0.1204$ *m*. The distances, $\Delta z$, from the surface and bottom boundaries to the center of the first cells are 0.098 *mm* and 1.96 *mm*, respectively. $Sc = 7$, $Pr = 7$.

[b] The number indicates $Re_*$ and the letters indicate *B*uoyancy or *N*o *B*uoyancy.

[c] W=0 for all cases.

constant heat flux boundary condition $\partial T/\partial z = Q_0/\lambda$ [*Soloviev and Schlussel*, 1994] where $Q_0 > 0$ and $\lambda$ is the thermal conductivity. The surface boundary condition for the scalar is a constant scalar concentration $S = S_0$, derived from the assumptions that (i) the air-water gas exchange is controlled by the water-side [*Jahne and Haussecker*, 1998] and (ii) the horizontal concentration gradients in the vicinity of the air-water interface are much smaller in the air than in the water, which is reasonable since the gas diffusivity coefficient is much larger in air than in water for $CO_2$ and $CH_4$ [*Don and Robert*, 2008]. The bottom boundary conditions for the temperature and the scalar are $\partial T/\partial z = \partial S/\partial z = 0$ which represent no heat or gas exchange through that boundary.

Finally, the flow is subject to periodic (cyclic) boundary conditions in the horizontal ($x$ and $y$) directions. We use $(u, v, w)$, $\theta$, and $s$ to represent the fluctuating parts of $(U, V, W)$, $T$, and $S$ respectively.

### 2.2. Solver and Discretization

The simulations are carried out using OpenFOAM which is an open-source parallelized computational fluid dynamics tool that uses a collocated finite volume approach, as described in more detail by *Fredriksson et al*. [2016]. It was chosen in order to eventually increase the problem complexity by introducing ripples and wind waves in future work.

The computational time step, $\Delta t$, is chosen with criteria associated with both the Kolmogorov time scale $t_K = (\nu/\varepsilon)^{1/2}$ [*Kundu et al*., 2012] and the Courant-Friedrichs-Lewy (CFL) number

$$\mathrm{FL} = \frac{\Delta t |U|}{\Delta l}, \tag{19}$$

where $|U|$ is the magnitude of the velocity through a cell where the length $\Delta l$ is in the direction of the velocity component. The constraint CFL $< 0.5$ in all cells results in $\Delta t \ll t_K$ and is therefore the limiting criteria for the time step.

The space discretization (mesh resolution) is thoroughly discussed by *Fredriksson et al*. [2016] for the cases driven by natural convection only. The same mesh resolution is used in the present work. The inclusion of surface shear causes larger structures at the surface such as elongated streaks (e.g., seen in Figures 1 and 2) that make a larger domain necessary. The surface shear, however, also increases the rate of turbulent kinetic energy dissipation resulting in smaller turbulence structures. Although the Kolmogorov, $\mathrm{L_K} = (\nu^3/\varepsilon)^{1/4}$, and Batchelor, $\mathrm{L_B} = \mathrm{Sc}^{-1/2}\mathrm{L_K}$, length scales are derived under the assumption of isotropic turbulence, and therefore must be used with caution for a flow driven by surface shear stress where the turbulence is far from isotropic, they can qualitatively be used to evaluate the mesh resolution. The results in *Fredriksson et al*. [2016] indicate that the scalar transport seems to be well captured, even for the case with $Sc = 600$, as long as the cell size is close to the size of the Batchelor length scale. This indicates that the scalar transport for a case with smaller Kolmogorov scale (case 240*B*) can be accurately captured as long as the Batchelor length scale is of the same magnitude ($Sc = 7$ in 240*B*). The mesh resolution can also be evaluated using the mesh resolution limits for DNS presented in *Grötzbach* [2013] as $h/L_K \leq 6.26$ and $h\ Pr^{3/4}/L_K \leq 3.45$ for the velocity and the temperature fields respectively. Here $h = (\Delta x \Delta y \Delta z)^{1/3}$ where $\Delta x$, $\Delta y$, and $\Delta z$ are the cell sizes in the $x$-, $y$-, and z-directions respectively. In the present study the average values of $h/L_K$ are 0.4, 0.5, 0.6, and 0.8 and $h\ Pr^{3/4}/L_K$ are 2.0, 2.2, 2.7, and 3.3 for case 0*B*, 120*B*, 180*B*, and 240*B* respectively which are below these limits. Case 240*B* has the highest surface shear stress and $Re_*$ and is therefore also as seen the most demanding case regarding the mesh resolution. Even this case has $h\ Pr^{3/4}/L_K$ below the limit for most of the depth with a local maximum of 3.5 well below the surface and a minimum of 2.2 in the vicinity of the surface respectively. The above analysis, and the fact that $Sc = Pr$, give reason to believe that the mesh resolution in the present study is appropriate to capture the physics of interest in this study.

We used the same mesh resolution for all the cases and the same domain size for all cases with surface shear stress in order not to impose the results. It is seen in the normalized results for RMS of the velocity and vorticity, the dissipation and the scalar concentration presented below that the results for case 120*NB* (largest elongated structures) and 180*NB* coincide very well. The exceptions are $v_{rms}$ and $\Omega_{x,rms}$ which have larger differences. The same trend in different $v_{rms}$ (transvers direction) can however be seen in the results in *Handler and Zhang* [2013] for a larger domain for comparable $Re_*$. This gives reason to believe that the domain is large enough to capture the processes of interest in this study.

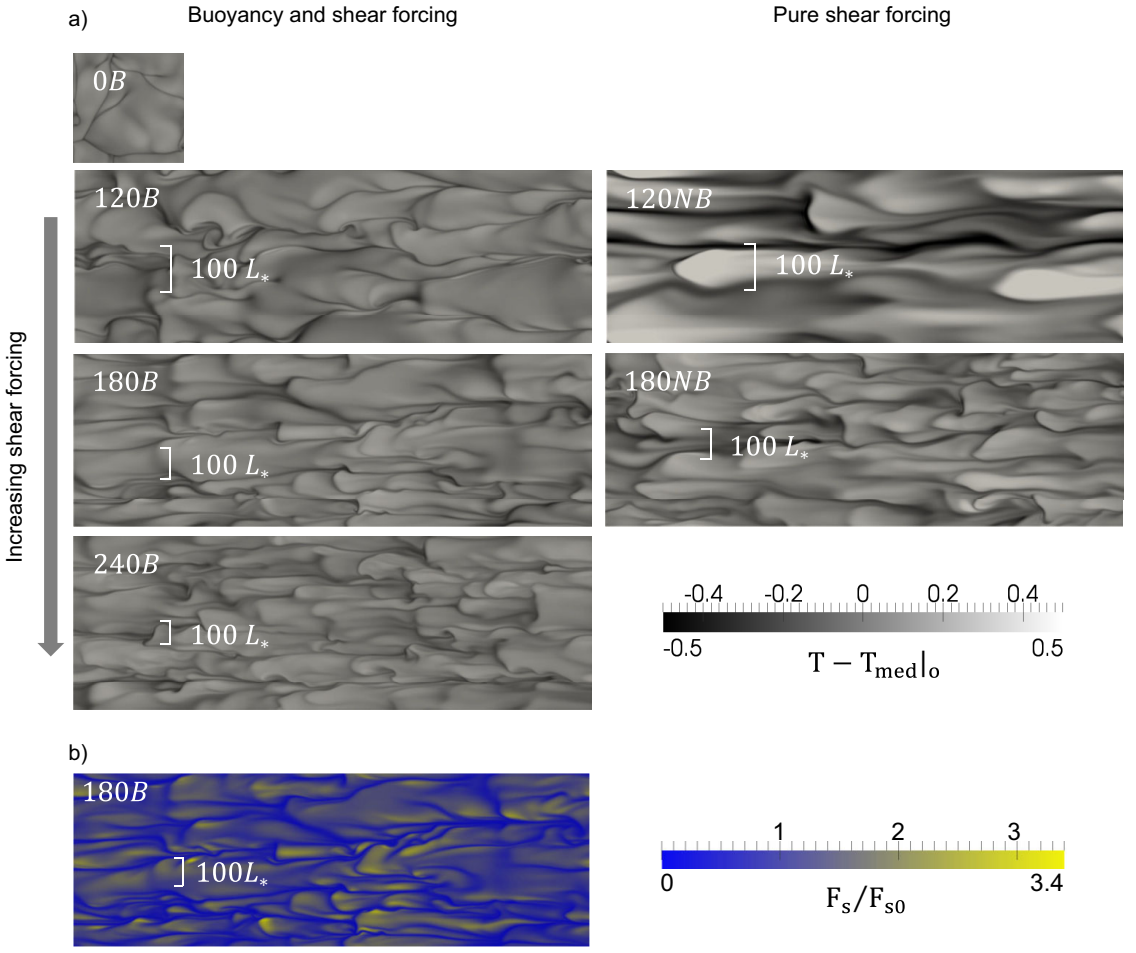


**Figure 2.** (a) Surface temperature and (b) scalar flux fields. The temperature is in centigrade with the median surface temperature as 0°. The same scaling is used for all subplots in Figure 2a and the temperature fields are within the limits (±0.5°C) for all cases but 120*NB* (±0.68°C). The length scale 100$L_*$, where $L_*=\nu/u_*$, is indicated in the subplots for cases with $u_* > 0$. The scalar flux in b) is normalized with the constant mean scalar flux.

The increased domain size results in approximately seven times more cells than for the case 0*B* in *Fredriksson et al.* [2016]. The results for RMS of the velocity and vorticity for the present case with no buoyancy and $Re_*=180$ and the results from *Handler and Zhang* [2013] agree well as discussed below. These results imply that the present code and numerical set-up give comparable results with their pseudo-spectral code and set-up.

### 2.3. Sampling Time

Sampling of the results is done under fully developed conditions, defined by steady mean and RMS values for all the sampled variables. Mean and RMS values are obtained by a combination of ensemble averaging and averaging over horizontal planes. The sampling is carried out for more than 20 large eddy time scales, $t^*$ and $t_{*,outer}$, for natural convection and shear driven flows, respectively, where $t_{*,outer}$ for the case 120*B* is the most conservative. This corresponds to more than 500 inner time scales $t^+$ or $t_{*,inner}$, for natural convection and shear driven flows respectively.

## 3. Results and Discussion

Section 3.1 presents a general overview of the flow for the different cases studied here, starting with a description of the temperature and scalar flux fields at the surface. Then the mean and RMS properties of the flow are presented together with a comparison with the DNS results from a pseudo-spectral code [*Handler and Zhang*, 2013]. Section 3.2 presents the scalar transfer velocities as a function of the friction velocity,

and discusses nondimensional relationships by presenting $k_{s,7}/u_* = \varphi_{III}(\ldots, Re_*, Ri)$, see equation (10). The parameterizations following equations (2)–(7) are then discussed in section 3.3. Finally section 3.4 presents new parameterizations of the transfer velocity as a function of *Sc*, *B*, and $u_*$.

The cases in the present study are summarized in Table 1. The cases are named with a number indicating the $Re_*$ number and the letters *B* or *NB* indicating *B*uoyancy or *N*o *B*uoyancy. Case 0*B* has previously been presented by *Fredriksson et al*. [2016] but is presented here as well in order to have flow cases ranging from buoyancy dominated to shear-stress dominated.

### 3.1. General Description of the Flow

Snapshots of the surface temperature and scalar surface flux are shown in Figure 2. The temperature fields show evidence of coherent structures characterized by thin streaks of descending cold water (dark in the figure) and larger areas or warmer ascending water between the streaks of cold water. It has previously [*Kim and Moin*, 1989; *Kim et al*., 1987] been shown that wall-bounded flows typically give streaky structures in the vicinity of the wall with a spanwise spacing of about $\lambda_* = 100L_*$. This spacing, sometimes referred to as the *streak spacing*, is shown by, e.g., *Handler et al*. [2001] using DNS and laboratory experiments to be present also for slip boundary conditions, and is therefore schematically shown in Figure 2a for reference. It is seen for the cases with no buoyancy (e.g., case 120*NB* and 180*NB*) that the streak-spacing in the temperature fields are decreasing with increasing friction velocity. An increasing friction velocity implies increasing $Re_*$ which in turn implies smaller turbulent scales and smaller streak spacing. This spacing-decrease scales well with $\lambda_*$. The temperature fields for the cases with buoyancy (e.g., 120*B* and 180*B*) are more complex with both finer and larger structures compared to the no-buoyancy cases. Furthermore, it can be seen that the streaks with cold water (dark in the figure) are much thinner for the cases with than without buoyancy indicating larger horizontal gradients of the temperature. These differences between cases with and without buoyancy appear to decrease for increasing $Re_*$, and they indicate a transition from a flow dominated by natural convection to one that is dominated by surface shear-stress. This transition can be understood by observing that for constant *B*, $\nu$, and *H*, an increasing $Re_*$ results in a decreasing *Ri* and, in turn, a decreasing *Ri* implies that the flow is less affected by buoyancy flux (or surface heat flux).

It is seen in Figures 2a and 2b that the warm spots (light colors in Figure 2a) coincide with areas of high surface-normal scalar-flux across the surface (yellow in Figure 2b). The intermediate case 180*B* is chosen to represent this phenomenon seen in all cases.

Figure 3 shows snapshots of the flow fields for the cases 120*B* and 240*B*. It can be seen that the areas with high surface-normal scalar flux coincide with thin diffusive boundary layers (i.e., areas with high scalar concentration close to the surface). High surface-normal scalar flux and thin diffusive boundary layers can also be seen to coincide with areas where the streamwise vorticity $\Omega_x$ is changing from a positive to a negative magnitude in the positive *y*-direction (spanwise diagonally from right to left in Figure 3). These areas are characterized by upwelling and divergence at the surface. Similarly it can be seen that areas of low scalar concentration and small surface-normal flux coincide with regions where $\Omega_x$ changes from a negative to a positive magnitude in the positive *y*-direction. These areas are characterized by downwelling and convergence at the surface. It is also shown that the scalar flux is more evenly spread out for 120*B* with smaller normalized scalar-flux variations than for 240*B*. The normalized scalar concentration variation is more pronounced in 240*B* compared to 120*B* (note the different scales in Figure 3). Since $F_{s0}/u_*$ is two times higher for 240*B* than for 120*B*, it can, however, also be concluded that the variation in the dimensional scalar concentration *s* is higher for 120*B* compared to 240*B*.

Figures 4 and 5 show the RMS values for the velocity, mean scalar concentration, rate of turbulent energy dissipation, and RMS of the vorticity

$$\Omega = \left(\frac{\partial w}{\partial y} - \frac{\partial v}{\partial z}, \frac{\partial u}{\partial z} - \frac{\partial w}{\partial x}, \frac{\partial v}{\partial x} - \frac{\partial u}{\partial y}\right). \tag{20}$$

Dimensional results are given in Figure 4 whereas shear scales have been used for the non-dimensional results for the cases with surface shear shown in Figure 5.

The RMS velocity and vorticity for the case 180*NB* are in Figures 4a–4f compared to the results for $Re_* = 180$ presented by *Handler and Zhang* [2013]. It can be seen that the results obtained from the present finite-

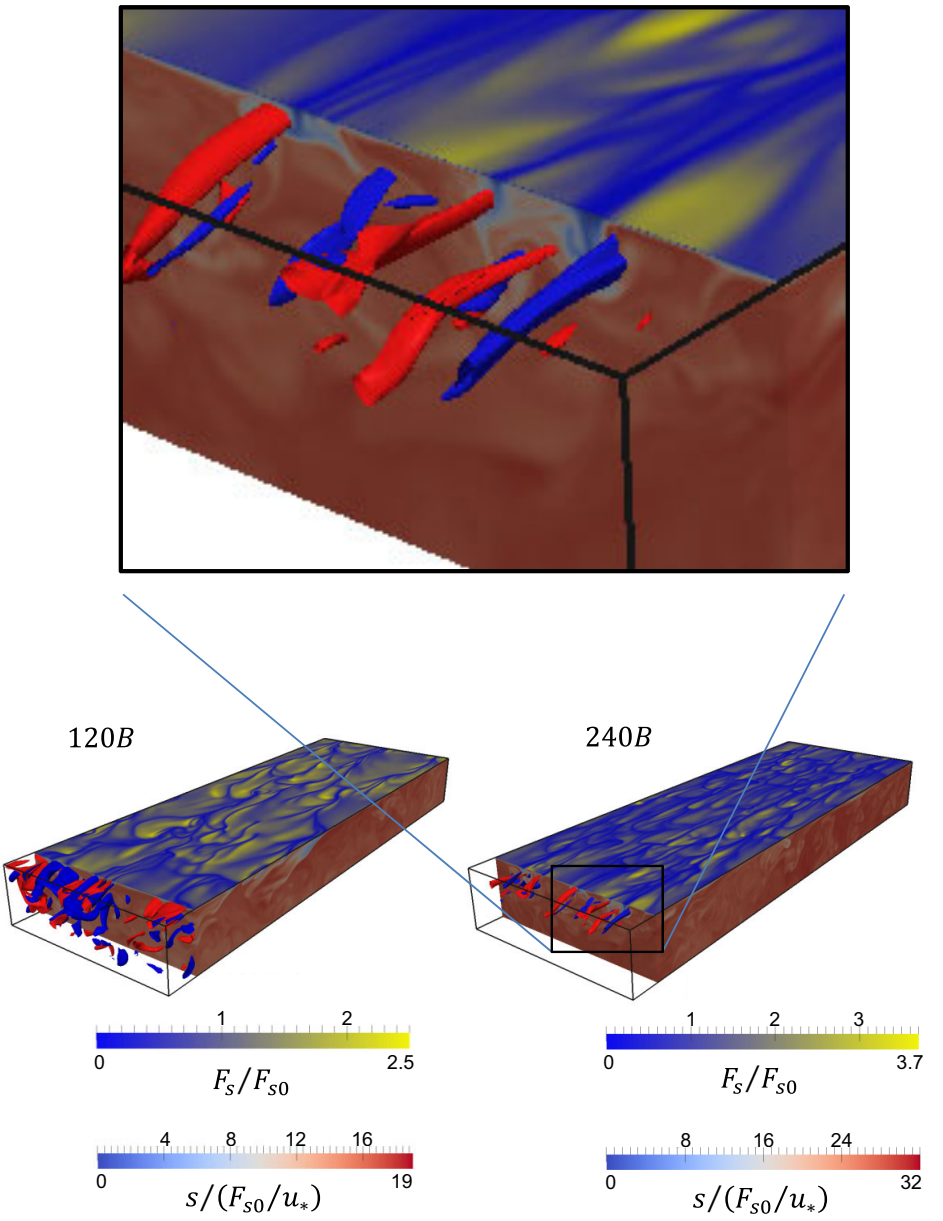


**Figure 3.** Snapshots for case 120*B* and 240*B*. Surface-normal scalar flux $F_s/F_{s0}$ at the surface and scalar concentration $s/(F_{s0}/u_*)$ inside the domain. Isosurfaces of normalized streamwise vorticity $\Omega_x/(u_*^2/\nu)$ equal $+0.25$ and $-0.25$ colored red and blue respectively. The visualizations of the scalar flux and the scalar concentration have been clipped in order be able to show the vorticity. Zoom-in of case 240*B*.

volume code closely follow the results from the pseudo-spectral code, which gives us confidence in the validity of our results for $w_{\mathrm{rms}}$, $\gamma_{\mathrm{rms}}$ and $\Omega_{\mathrm{rms}}$ which are of high importance for air-water gas exchange [e.g., *Fredriksson et al*., 2016; *Handler and Zhang*, 2013; *Ledwell*, 1984].

Furthermore, Figures 4a–4f show that the RMS of the velocity and vorticity increase with increasing surface shear stress. The influence of buoyancy forcing is seen to decrease the streamwise RMS velocity and spanwise RMS vorticity, and increase the spanwise RMS velocity near the surface, thus causing a more horizontally isotropic field with buoyancy forcing than without. Figure 4g shows the rate of turbulent energy dissipation. It is seen that the maximum dissipation for each case increases dramatically with increasing surface stress, and that the values with and without buoyancy forcing are of similar magnitude. The figure shows both the true viscous dissipation

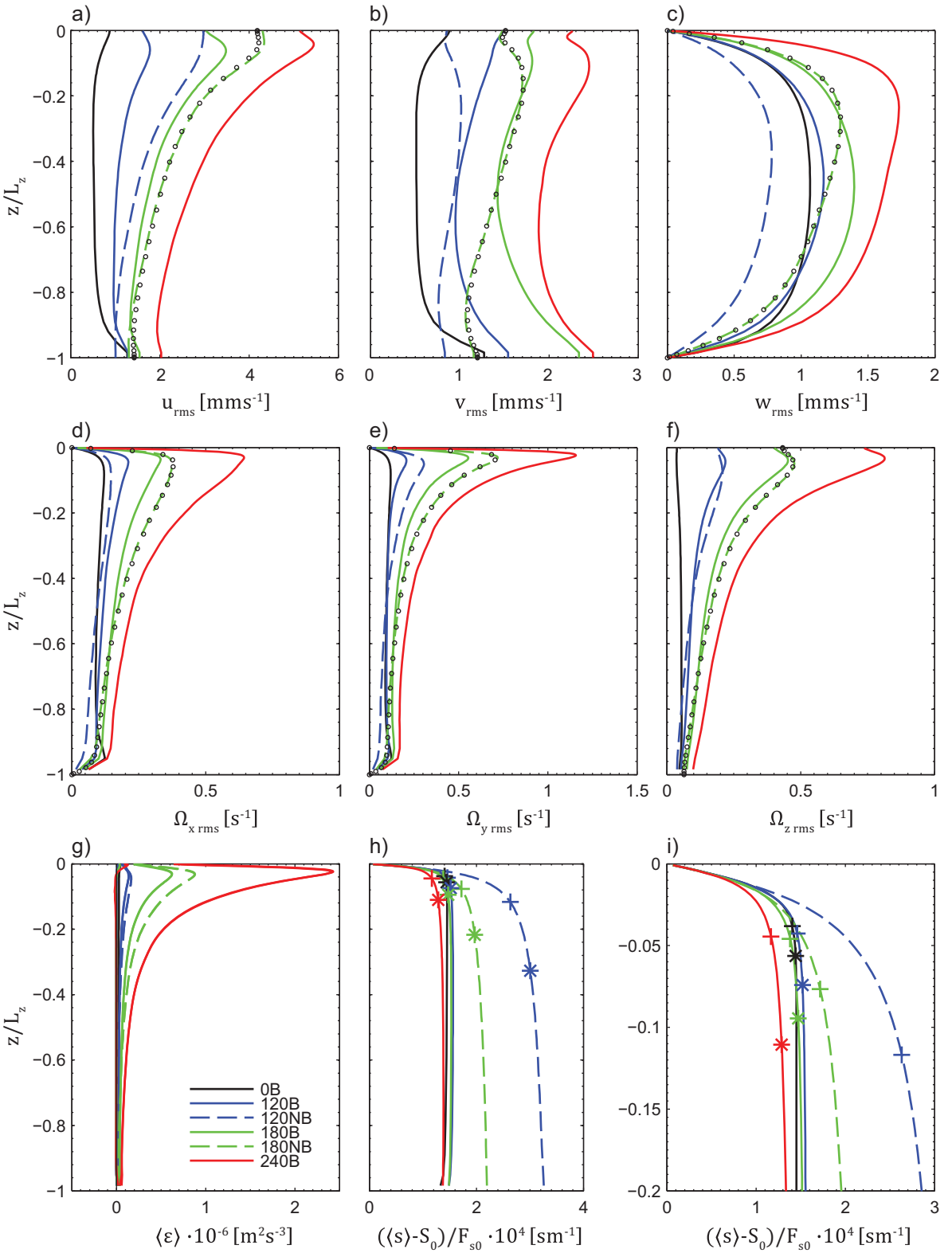


**Figure 4.** Flow statistics for present model and the results from a pseudo-spectral method [*Handler and Zhang*, 2013] for $Re_* = 180$ with no buoyancy. The pseudo-spectral results are denoted with markers given at every fourth vertical node. (a–c) RMS of the velocity $u$, $v$, and $w$. (d–f) RMS of the vorticity $\Omega_x$, $\Omega_y$, and $\Omega_z$. (g) Rate of turbulent kinetic energy dissipation. (h) Mean scalar concentration profiles normalized with scalar flux $F_{s0}$. (i) Zoom of mean scalar concentration profiles normalized with scalar flux $F_{s0}$.

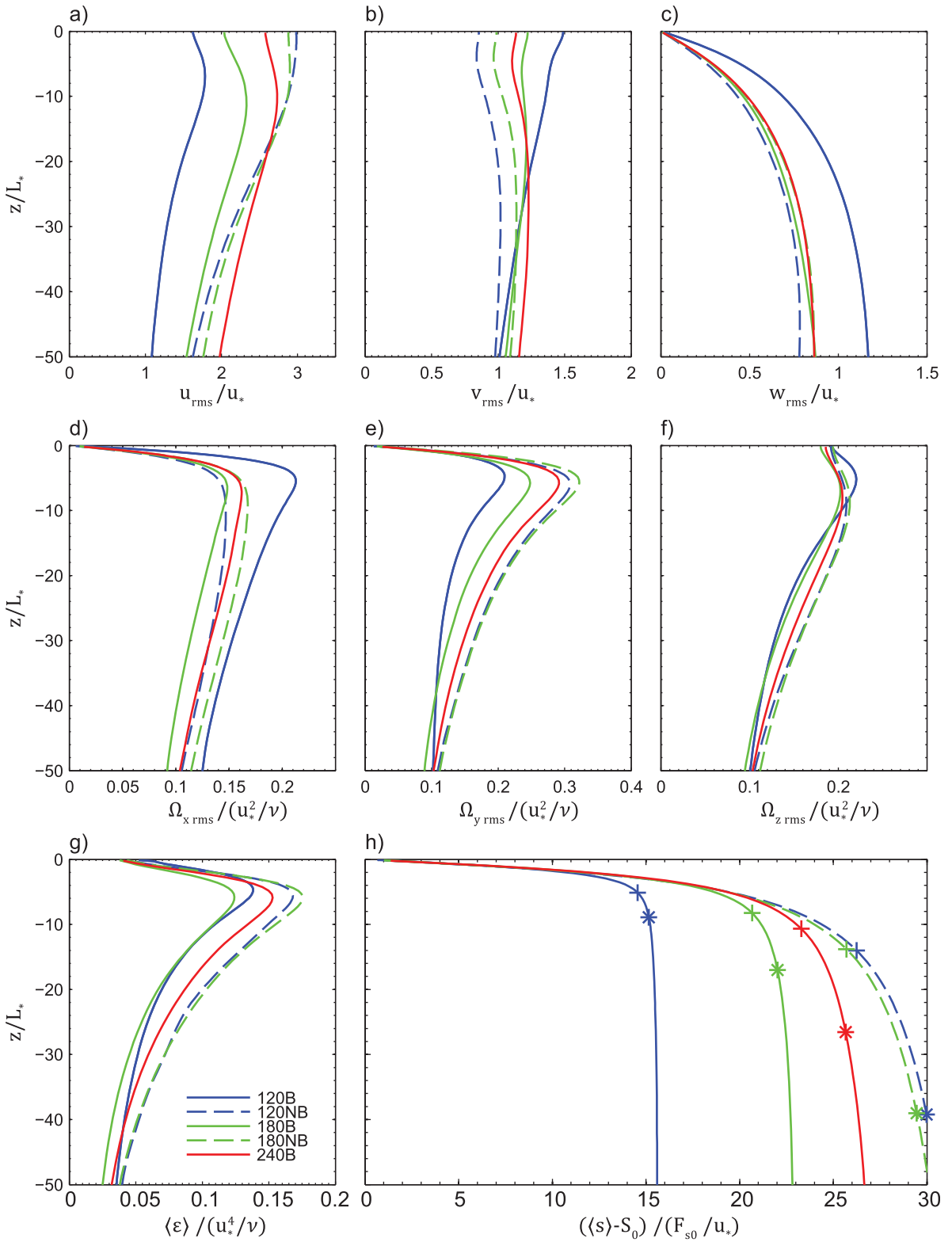


**Figure 5.** Flow statistics. (a–c) RMS of the velocity $u$, $v$, and $w$ normalized with $u_*$. (d–f) RMS of the vorticity $\Omega_x$, $\Omega_y$, and $\Omega_z$ normalized with $u_*^2/\nu$. (g) Rate of turbulent kinetic energy dissipation normalized with $u_*^4/\nu$. (h) Mean scalar concentration profiles normalized with $F_{s0}/u_*$.

$$\varepsilon = \nu \frac{\partial u_i}{\partial x_k} \frac{\partial u_i}{\partial x_k} + \nu \frac{\partial u_i}{\partial x_k} \frac{\partial u_k}{\partial x_i} \tag{21}$$

and the pseudo-dissipation, $\tilde{\varepsilon}$, defined as the first term in equation (21). Equation (21) is written in tensor notation where the subscripts $\langle . \rangle_i$ and $\langle . \rangle_k$ mean summations over the three velocity components ($u$) and coordinate directions ($x$). The pseudo-dissipation is sometimes referred to as the isotropic dissipation which is somewhat misleading in these simulations since the dissipation is far from isotropic close to the surface even when $\tilde{\varepsilon}$ equals $\varepsilon$. This is especially true for the shear-only cases and the combined driven flow cases where the components $\nu\left(\frac{\partial u}{\partial z}\right)^2$ and $\nu\left(\frac{\partial u}{\partial y}\right)^2$ dominate. Furthermore, both $\tilde{\varepsilon}$ and $\varepsilon$ increase dramatically close to the surface and reach maximum values and then decreases with increasing depth.

The mean scalar concentrations are shown in Figure 4h. The profiles are similar both in magnitude and in shape for the three cases with buoyancy forcing and the weakest wind forcing (case 0*B*, 120*B*, and 180*B*). These cases, with $Ri > 0.01$, all have well-defined bulk scalar-concentration with a zero vertical gradient below the diffusive boundary layer. The two cases without buoyancy (120*NB* and 180*NB*) and the case with buoyancy forcing and the strongest shear-stress forcing (240*B*) are similar in shape but not in magnitude. It can be seen that the scalar concentration difference needed to maintain the surface scalar-flux is decreasing with increasing surface shear stress for these cases. Hence the transfer velocity increases with increasing friction velocity (increasing wind speed).

The scalar diffusive boundary-layer thickness, $\delta_{s,7(5\%)}$ ($\delta_{s,7(1\%)}$), is defined as where the diffusive transport accounts for 5% (1%) of the total scalar transport, where the 5% definition follows the work of *Leighton et al*. [2003]. In Figure 4h, $\delta_{s,7(5\%)}$ are indicated with + and $\delta_{s,7(1\%)}$ are indicated with *. The diffusive boundary layer thickness is often [e.g., *Jahne and Haussecker*, 1998] defined on the basis of where the gas concentration gradient close to the surface intersect the vertical line of a bulk value (with zero vertical gradient). It is, however, hard to meet this definition when the bulk magnitude is not clearly defined. We argue that the definition using 5% gives a diffusive boundary-layer thickness more indicative of where the diffusive boundary layer actually ends, whereas the definition with 1% gives thicknesses below the typical diffusive boundary layer thickness. Hence, $\delta_{s,7} = \delta_{s,7(5\%)}$ if not further specified. This diffusive boundary layer thickness is then used to estimate the concentration difference needed to maintain the scalar flux and used to calculate the gas transfer velocity. The largest transfer velocity differences for the two definitions of $\delta_{s,7}$ are found for the cases with no buoyancy forcing. The differences between $k_s$ using the diffusive layer definition of 5% and 1% are however less than 10%.

Figure 5c shows that the scaling with friction velocity collapses the RMS of the vertical velocity, $w_{rms}$, well for the cases without buoyancy. The friction velocity scaling collapses $u_{rms}$ and $v_{rms}$ fairly well although $v_{rms}/u_*$ decreases for decreasing $Re_*$. This decrease is consistent with the results presented by *Handler and Zhang* [2013]. For the cases with buoyancy, $u_{rms}/u_*$ is lower whereas $v_{rms}/u_*$ is higher than the cases with no buoyancy. $w_{rms}/u_*$ is higher for $Re_* = 120$ but almost the same for $Re_* = 180$ for cases with buoyancy forcing. The differences in the normalized RMS velocities for the buoyancy cases compared to no-buoyancy cases are thus more pronounced for lower than higher $Re_*$ (and thus more pronounced for higher $Ri$). The higher $w_{rms}/u_*$ for 120*B* is a result of the RMS of the vertical velocity still being influenced by the natural convection, so that a scaling with only the friction velocity fails to collapse the results. This can also be seen in Figure 4c where the dimensional values of $w_{rms}$ close to the surface can be seen to coincide for 0*B* and 120*B*.

The normalized RMS vorticity is shown in Figures 5d–5f. The scale used for normalization is the inverse shear time scale as $\Omega_* = 1/t_* = u_*^2/\nu$. It is seen that $\Omega_*$ collapses the RMS vorticity well in all directions for the no buoyancy cases (120*NB* and 180*NB*) and fairly well for case 240*B*. Furthermore, it is seen that $\Omega_*$ collapses $\Omega_{z,rms}$ and to some extent $\Omega_{x,rms}$ for the combined-driven cases 120*B* and 180*B*. This is not the case for $\Omega_{y,rms}$ which decreases with decreasing shear stress. Once again the results for case 240*B* are more similar to the pure-shear driven cases than the flow cases with higher $Ri$.

Also for the dissipation rate (Figure 5g), the cases without buoyancy forcing are collapsed by shear-based scaling. Surprisingly, the cases with buoyancy forcing give smaller normalized dissipation rates although the total forcing increases. An intuitive expectation might be that the dissipation due to buoyancy forcing adds to the dissipation due to shear forcing, but the results show that the buoyancy forcing actually decreases the dissipation caused by pure shear forcing. However, it is seen that the normalized dissipation for the case with lower $Ri$ (240*B*) approaches the normalized dissipation for the *NB* cases. Very near the

surface, within the viscous boundary layer, the differences between the *B* and *NB* cases are not as pronounced as below the viscous boundary layer.

Figure 4i is a zoom of Figure 4h. Here it can be seen that the boundary thicknesses, $\delta_{s,7}$, are similar for the cases 0*B*-240*B*. It can, however, additionally be seen that $\delta_{s,7}$ for 240*B* follows the trend for the *NB* cases with decreasing $\delta_{s,7}$ for increasing $Re_*$. It can thus be concluded for 240*B* that $\delta_{s,7}$ follows the trends for both the *B* and *NB* cases, indicating that this case is in a transition between buoyancy driven and shear driven forcing. Furthermore, it can be seen that $\Delta\bar{s}\ \left(\delta_{s,7}\right)$,used for the calculation of transfer velocity, follows these trends as well. It is shown in Figure 5h that the shear scales collapse the diffusive boundary thicknesses and scalar concentrations very well for the no-buoyancy cases 120*NB* and 180*NB* and to some extent also 240*B*. Our interpretation is here that the transition from buoyancy-dominated to shear-stress-dominated scalar-transfer starts between case 180*B* and 240*B*.

### 3.2. Scalar Transfer Velocity as a Function of the Friction Velocity

The scalar transfer velocity $k_{s,7}$ is shown in Figure 6. The concentration difference needed to calculate the transfer velocity is defined as the concentration difference over the diffusive boundary thickness $\delta_{s,7}$ (Figure 4h). Figure 6 shows for the shear-only driven cases (120*NB* and 180*NB*) that the transfer velocity are in a reasonable agreement with, being proportional to the friction velocity according to the expression

$$k_g = A_\chi u_* Sc^{-n},\quad A_\chi = 8.9^{-1} \tag{22}$$

from the experimental work of *Jahne et al.* [1987], which is given in Figure 6 for reference. This expression was found for friction velocities ranging from the highest friction velocity in present study and upward. Buoyancy effects, if any, are here therefore assumed to be limited. Equations (2) and (3) are presented in Figure 6 referenced to $Sc=7$ with $n=1/2$ since the use of $n=1/2$ is common practice and therefor of interest in this study. The value of $n$ can, however, vary especially during low wind conditions shown in numerous studies [e.g., *Fredriksson et al.*, 2016].

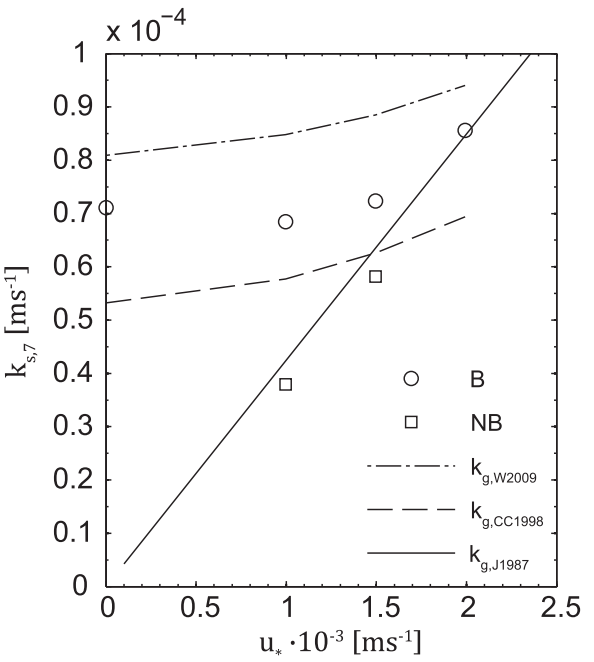


**Figure 6.** The scalar transfer velocity $k_{s,Sc}=F_{s,Sc}/\Delta s_{Sc}$ where $\Delta s_{Sc}$ is defined as the scalar concentration difference between the surface and at the diffusive boundary layer thickness. Round markers denote cases with combined forcing and squares denote cases with pure shear stress forcing. The dashed and dash-dotted lines denote the wind parameterizations according to equations (2) and (3), referenced to $Sc=7$ with $n=1/2$. The solid line denotes a linear increase of the transfer velocity as a function of the friction velocity [*Jahne et al.*, 1987].

The transfer velocity for the cases with combined forcing is roughly constant up to a friction velocity $u_* \approx 1.5\ mm\ s^{-1}$ for the surface heat flux $Q_0=100\ Wm^{-2}$. It can, however, be seen that the transfer velocity is slightly smaller for 120*B* than for 0*B*. This is interesting since the total forcing and the dissipation are increasing. The flow dynamics and consequently the scalar transfer are here, however, in transition from being driven by natural convection (plumes) to shear stress (mainly streamwise vorticity). We hypothesize that the shear in this intermediate flow situation inhibits the efficiency of the scalar transfer from the plumes but still is not sufficiently strong to fully initiate the scalar transport from streamwise vorticity. This process is however not fully understood at this stage. For the same cases there is a large increase in dissipation rates with increasing friction velocity (Figure 4g). This increase in dissipation rates without an associated increase in transfer velocity is problematic for the dissipation parameterization (equation (5)), since this parameterization predicts increasing transfer velocities with increasing dissipation rates, and will be discussed further in section 3.3. For higher friction

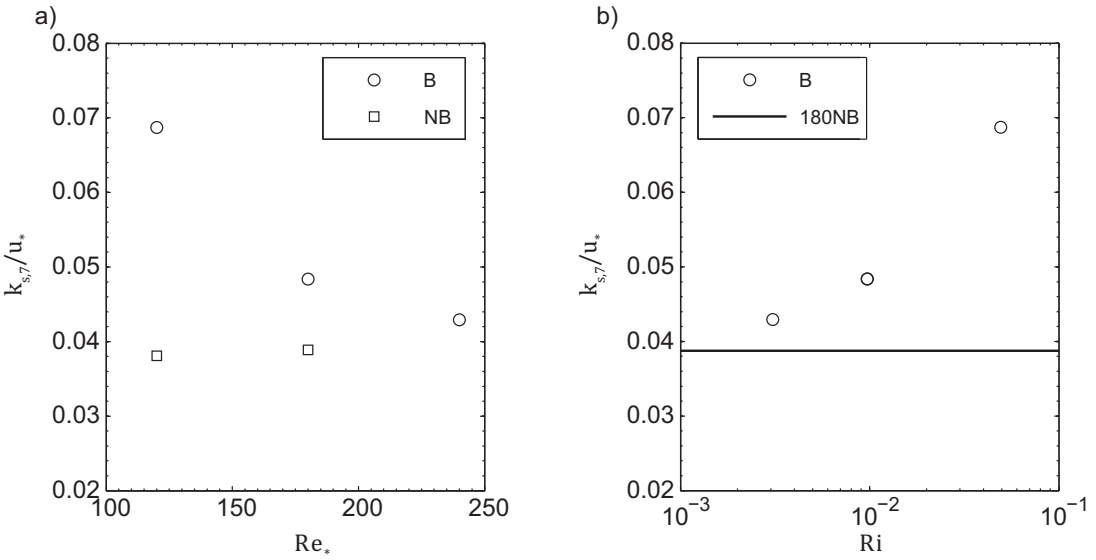


**Figure 7.** The normalized transfer velocity $k_{s,7}/u_*$ according to equation (10) as a function of (a) $Re_*$ and (b) $Ri$.

velocities ($u_* > 1.5mm\ s^{-1}$) the transfer velocity for the combined cases is seen to approach the linear increase associated with the purely shear driven cases, which is an indication that these cases are increasingly dominated by the surface shear stress.

The difference in the coherent structures in the temperature field at the surface, between cases with and without buoyancy forcing is larger for $Re_*$=120 (cases 120*B* and 120*NB*) than for $Re_*$ =180 (cases 180*B* and 180*NB*), see Figure 2. Furthermore, Figure 5 shows that the normalized RMS velocity and vorticity, dissipation and mean scalar concentration for case 240*B* is closer to the results for the pure shear cases than 180*B* is. This indicates a corresponding transition in the transfer velocity characteristics as also seen in Figure 6. We will now use the non-dimensional transfer velocity $k_{s,7}/u_*$ as a function of both $Re_*$ and $Ri$ in order to further study this transition. Figure 7a shows the dependency of $Re_*$ for all the cases that are driven by surface shear stress and Figure 7b shows the dependency of $Ri$ for all the cases that are driven by both surface shear stress and buoyancy flux. It is seen in Figure 7a that the two cases without buoyancy have $k_{s,7}/u_*$ values of similar magnitude, and that these values also are similar to the values for the cases with buoyancy forcing for large $Re_*$, i.e. the cases where we expect the least influence of buoyancy. The cases without buoyancy can also be seen as limiting cases for infinitesimal small $Ri$ numbers and therefore set a minimum magnitude of $k_{s,7}/u_*$, here drawn as a straight line in Figure 7b. It can be seen that $k_{s,7}/u_*$ is decreasing toward this minimum magnitude of $k_{s,7}/u_*$ for decreasing $Ri$. We therefore conclude that the variation in $k_{s,7}/u_*$ for the cases with buoyancy is a $Ri$ number effect. Furthermore, it is seen that the buoyancy does influence $k_{s,7}/u_*$ at least down to $Ri \approx 0.003$ (240*B*) but to a continuously smaller degree.

### 3.3. Parameterizations of Mass Transfer Velocity

The scalar transfer velocity, $k_s$, is used to study the parameterization methods by expressing the transfer velocity coefficients in equations (5)–(7) as

$$A_{diss} = \frac{k_{s,Sc}}{(\varepsilon\nu)^{1/4}} Sc^n, \tag{23}$$

$$A_{div} = \frac{k_{s,Sc}}{\sqrt{\gamma_{rms}}\,\nu} Sc^n, \tag{24}$$

and

$$A_{heat} = \frac{k_{s,Sc}}{\kappa_{heat}} \left[\frac{Sc}{Pr}\right]^n \tag{25}$$

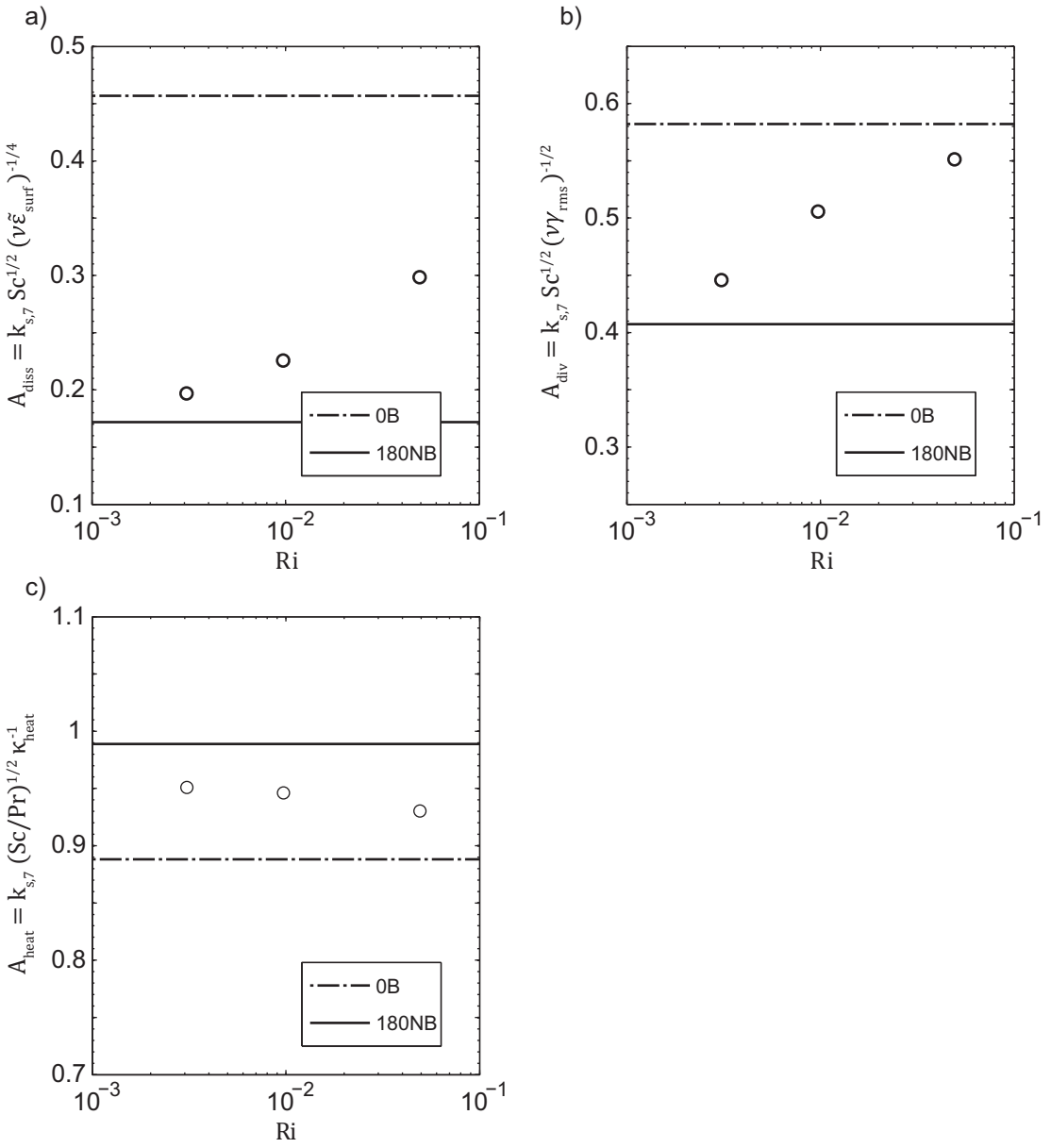


**Figure 8.** Transfer velocity coefficients following equations (5)–(7) as a function of *Ri* for (a) $A_{diss}$, (b) $A_{div}$, and (c) $A_{heat}$. The solid and dash-dotted lines denote the transfer velocity for 180 *NB* and 0*B* respectively. These cases represent the limiting cases for $Ri \to 0$ and $Ri \to \infty$, respectively.

with $n=1/2$. This exponent was found to work well for a slip boundary condition during natural convection by *Fredriksson et al.* [2016]. The coefficients $A_{diss}$, $A_{div}$, and $A_{heat}$ are discussed in the sections 3.3.1-3.3.3 and plotted in Figure 8.

### 3.3.1. Rate of Turbulent Kinetic Energy Dissipation

The turbulent kinetic energy dissipation used in equation (5) is, as in *Fredriksson et al.* [2016], the pseudo-dissipation at the thickness of the viscous sublayer. This thickness is defined as the smallest depth where the non-isotropic part of the dissipation is zero which also means that $\varepsilon$ equals $\tilde{\varepsilon}$. This value is close to the maximum dissipation for all the cases with surface shear.

It can be seen in Figure 8a that $A_{diss}$ increases with increasing *Ri*, and that the variation is large, with the pure shear case (180*NB*) having a value less than half of that for pure buoyancy forcing (0*B*). This is a reflection of what we have seen above (section 3.1 and 3.2) that the cases with combined forcing

tend to have higher $k_s$ and smaller dissipation rates than their corresponding cases without buoyancy forcing. This implies in turn that the transfer parameterization based on dissipation must be used with caution.

#### 3.3.2. Surface Flow Divergence

$A_{div}$ shown in Figure 8b is computed using $\gamma_{\mathrm{rms}}$ at the surface. It can be seen that $A_{div}$ and $A_{diss}$ show a similar functional relationships to $Ri$ with a decreasing magnitude of the transfer-velocity coefficient for decreasing $Ri$. The relative variation $\left(A_{div,\max}-A_{div,\min}\right)/A_{div,mean}$ is though much smaller than $\left(A_{diss,\max}-A_{diss,\min}\right)/A_{diss,mean}$ which implies that the parameterization method based on surface flow divergence is more robust for different kinds of flow forcing than the one based on rate of turbulent kinetic energy dissipation. Equation (7) with $A_{div}=0.5$ estimates the transfer velocity $k_{s,7}$ for the whole range of $Ri$ numbers with a deviation $\approx$ 15%.

#### 3.3.3. Heat Transfer Velocity

The temperature difference $\Delta T$ used in equation (7) is in the present study defined as the difference between the temperature at the surface and at the thermal boundary layer thickness. The thermal boundary layer thickness is defined similarly to the diffusive boundary layer thickness. It is shown in Figure 8c that the heat transfer velocity is a better proxy for the scalar transfer velocity compared to the dissipation and the divergence. The relative variation of $A_{heat}$ for *0B* to 240B is approximately 10% where the variation for the parameterizations based on divergence approximately 15% and dissipation is more than 35%.

#### 3.3.4. Wind Parameterizations

The parameterizations based on wind speed are using the wind speed at 10 m height, $U_{10}$. This wind speed needs to be converted into $u_*$ in order to be able to compare these parameterizations with the results shown in Figure 6. $U_{10}$ is here converted [e.g., *Csanady*, 2001] into air-side friction velocity $\mathrm{u}_{*\mathrm{a}}$ using

$$\frac{\mathrm{U(z)}}{\mathrm{u}_{*\mathrm{a}}}=\kappa^{-1}\ln\left(\frac{u_{*a}\ z}{\nu_{\mathrm{a}}}\right)+5.7, \tag{26}$$

which is assumed valid for neutral conditions. Here, the subscript $a$ denotes the air-side. The waterside friction velocity is then found by $u_*=\ u_{*a}(\rho_a/\rho)^{1/2}$. The transfer velocities for the different $Sc$ numbers in equations (2) and (3) are converted using equation (4) with $n=1/2$.

It is shown that both wind parameterizations in equations (2) and (3) give results similar to the results for the combined driven cases where $k_{g,W2009}$ [*Wanninkhof et al*., 2009] overestimates and $k_{g,CC1998}$ [*Cole and Caraco*, 1998] underestimates the transfer velocity compared to the present results. The disagreement between present results and the estimates according to $k_{g,W2009}$ and $k_{g,CC1998}$ can however also be seen as if $k_{g,W2009}$ is adopted for higher heat fluxes and $k_{g,CC1998}$ for lower heat fluxes than used in the present study. Both these empirical parameterizations predict that there is a scalar transfer also for low-wind conditions which, as in the present DNS, may be caused by natural convection. This disagrees with some other wind parameterizations [*Bade*, 2009] with a zero transfer velocity for no-wind conditions. For higher wind speeds and $Sc=7$, at least $k_{g,CC1998}$ underpredicts the influence of wind stress compared with the present results and those of *Jahne et al*. [1987].

#### 3.3.5. Gas Transfer Resistance Below the Diffusive Boundary Layer

The transfer velocity has so far in sections 3.2 and 3.3 been limited to the resistance to transfer due to the diffusive boundary layer. The scalar concentration difference has been defined as the concentration difference, $\Delta_{s,\ BL}$, between the surface and the diffusive boundary thickness. In practice, the gas transfer velocity is based on the gas concentration difference from the surface to a bulk value (or the mixed layer concentration) assuming a zero vertical concentration gradient in the mixed layer. An actual bulk value is, however, not present for a flow situation dominated by shear as can be seen in Figures 4h and 5h. On the other hand, this effect is small for typical greenhouse gases such as $CO_2$ and $CH_4$ with the $Sc$-numbers approximately two magnitude higher than in the present study [*Jahne and Haussecker*, 1998]. For these gases, the resistance over the diffusive boundary layer dominates the gas-exchange resistance, and the $\sim$10% concentration increase we see outside the diffusive boundary layer for $Sc\ =\ 7$ will decrease to $\sim$1% for $Sc=600$.

The buoyancy flux is in the present study specified via the surface heat flux $Q_0$. For natural conditions, this heat flux includes latent, sensible, and net long-wave radiative heat fluxes that all originate from the uppermost molecular layers of the water. The short-wave solar radiation, however, penetrates the air-water interface where the penetration depth is a function of e.g., absorption coefficient and radiative power [*Fairall et al*., 1996; *Garbe*, 2001; *Jerlov*, 1976]. The varying absorption gives that the buoyancy flux can be negative in some layers of the water column (usually in the surface water) for certain conditions. Typical conditions

can be weak winds and high solar short-wave radiation or cloudy conditions with warm air above cold water. A negative buoyancy-flux is stabilizing the stratification and the concentration gradients will in this layer be larger than for a positive buoyancy flux (unstable conditions). In turn, this results in a decrease of the transfer velocity based on the bulk concentration. These stratification processes is though beyond the scope of the present study where we focus on the processes that influence the gas transfer velocity in the near-surface layer. The spatially and temporally constant source term $\phi_T$ used in the thermal energy equation (17) can be seen to represent a case where the short-wave absorption is evenly distributed in the vertical direction including night time conditions with very limited short-wave radiation.

### 3.4. Parameterizations of the Gas Transfer Velocity as a Function of *Sc*, *B*, and $u_*$

It is shown in Figures 2–8 that there is a transition from buoyancy to surface-shear-stress dominated air-water exchange. Our first hypothesis is that the forcings that control the gas flux are additive whereas our second hypothesis is that it is either the forcing from buoyancy or from shear-stress that controls the gas flux. The assumption that the dissipation from the two types of forcing is additive was shown in Figure 4g to be problematic. However, from a pure dimensional argument it still seems reasonable and the transfer velocity can then be modeled as

$$k_{g,sum} = \left(A_1 B\nu + A_2 u_*^4\right)^{1/4} Sc^{-n} \tag{27}$$

where the coefficients $A_1 = \left(A_{Buoy}\right)^4$ and $A_2 = (A_{Shear})^4$, respectively. Here $A_{Buoy} = 0.4$ is the transfer velocity coefficient for buoyancy driven flows [*Fredriksson et al*., 2016] and $A_{Shear} = 0.1$ is the transfer velocity coefficient for shear-stress driven flows in the expression $k_{s,shear} = A_{shear} u_* Sc^{-n}$ using origin and $k_{s,7}$ for 120*NB* and 180*NB*. Equation (27) originates from the dissipation parameterization (equation (5)) and uses that the forcing from buoyancy and shear scale as *B* and $u_*^4/\nu$, respectively. Equation (27) can be rearranged to give

$$k_{g,sum} = A_{Shear} u_* (Ri/Ri_c + 1)^{1/4} Sc^{-n}, \quad Ri_c = \left(A_{Shear}/A_{Buoy}\right)^4 \tag{28}$$

where the critical Richardson number $Ri_c \approx 4 \cdot 10^{-3}$. We have here extrapolated the results from *Fredriksson et al*. [2016] that $A_{Buoy}$ is the same for both no-slip and slip surface boundary condition to be valid also for the sheared cases. This extrapolation needs to be verified in future DNS since it is contradictory to some experimental results [*Jahne et al*., 1987], who find that the shear constant depends on the surface contamination for shear driven gas flux.

The simplest parameterization according to our second hypothesis is to use the expression for the buoyancy forced gas flux down to a critical Richardson number and then switch to the expression for the gas flux forced by shear-stress. This can be expressed as

$$k_{g,tres} = A_{Buoy} (B\nu)^{1/4} Sc^{-n}, \quad Ri > Ri_c \tag{29}$$

$$k_{g,tres} = A_{Shear} u_* Sc^{-n}, \quad Ri < Ri_c$$

Another way to model the transfer velocity under the second hypothesis is to assume that transition from buoyancy to shear-stress controlled gas flux can be modeled with an error function

$$\mathrm{erf}(x) = \frac{2}{\pi} \int_0^x e^{-t^2} dt \tag{30}$$

often used to model step functions from one state to another. The total scalar transfer velocity can then be expressed by

$$k_{g,erf} = \left[ A_{Buoy} (B\nu)^{1/4} erf\left(\frac{Ri}{Ri_{c,erf}}\right) + A_{Shear} u_* \left(1 - erf\left(\frac{Ri}{Ri_{c,erf}}\right)\right)\right] Sc^{-n}. \tag{31}$$

Here $Ri_{c,erf} = 0.01$ is a critical *Ri* number which defines the *Ri* number at which the transition takes place. The advantages with equations (28) and (31) compared to equation (29) are that they are defined in a single expression.

Figure 9 shows both equations (28) and (29) for a set of different buoyancy forcings corresponding to $Q_0 = 50,\ 100$, and 200 $\mathrm{Wm}^{-2}$ (the case with $Q_0 = 100$ is marked with a thicker line). The two cases for pure natural convection with $Q_0 = 50$ and $Q_0 = 200$ marked with filled markers were part of the study

presented by *Fredriksson et al.* [2016]. It can be seen that equation (28) overestimates and (29) underestimates the transfer velocity. The error-function parameterization in equation (31) gives a maximum error of 20% while the other two parameterizations have estimation errors of less than 10%.

The additive gas transfer velocity $k_{g,sum}$ is in Figure 10 presented as a function of *U10* for $Sc=600$ for $n=1/2$ and $2/3$ representing a clean surface and a surface with surfactants. $k_{g,W2009}$ is calculated for $Sc=600$ using equation (4) with $n=1/2$. The friction velocity, $u_*$, has been converted into the wind speed, $U_{10}$, using equation (26). The friction velocities for the cases in this paper correspond to wind speeds up to $U_{10} \approx 2\ m\ s^{-1}$ coinciding with the wind speed where microscale breaking waves start to develop, whereas Figure 10 covers $0 < U_{10} < 5\ m\ s^{-1}$. The transfer velocities using $k_{g,sum}$ have thus been extrapolated outside the area that covers the forcing conditions for the cases performed in this study. The extrapolation is done in order to study how the proposed parameterizations compare with parameterizations based on the wind speed. It is shown that the results of Jähne et al (1987) that includes the effect of microscale breakers does not predict much larger gas transfer velocities than we predict for a pure shear forced surface which is relevant to notice for future work. The buoyancy effect is seen to be small for wind velocities larger than 3 $ms^{-1}$. This means that these results do not support buoyancy-enhanced gas fluxes reported at higher wind speeds [e.g., *Rutgersson and Smedman*, 2010].

## 4. Summary and Conclusions

Air-water gas- and heat-exchange enhanced by natural convection and wind are studied using DNS. The gas transfer is modeled with a passive scalar ($Sc=7$) with a constant concentration boundary condition at the surface. The wind forcing is modeled using a constant shear stress boundary condition at the surface. The present finite-volume method is shown to agree well with a pseudo-spectral method for comparable cases, which implies that the results are robust for these two codes. The present DNS work is a continuation of the work presented by *Fredriksson et al.* [2016]. The mesh resolution is the same, given the extensive mesh sensitivity analysis performed in that work. The computational domain is however extended in the streamwise and spanwise directions in order to enable accurate modeling of the wind shear-stress effects.

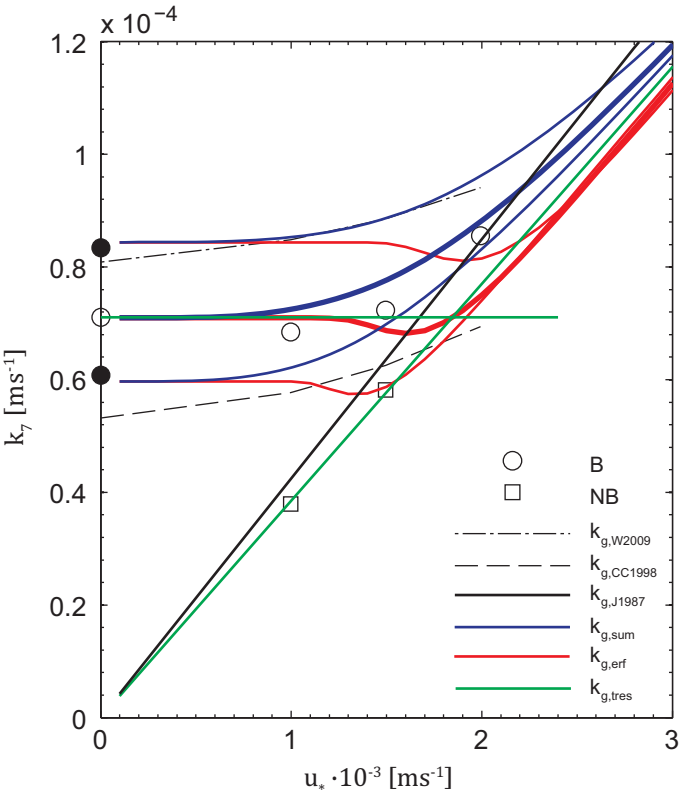


**Figure 9.** The gas transfer velocity $k_{g,7}$ according to equations (28) with green and (31) red line for $Q_0 =$ 50, 100, and 200 $Wm^{-2}$. The scalar transfer velocities, $k_{s,7}$, for cases presented in Table 1 are marked with circles, and for pure buoyancy forcing with $Q_0 =$ 50 and 200 $Wm^2$ are marked with filled circles. The latter cases were presented by *Fredriksson et al.* [2016]. The transfer velocities according to equation (29) for the pure buoyancy (shear) forcing are indicated in yellow.

The surface, which is subject to constant shear stress which together with the results from the case with slip boundary condition presented by *Fredriksson et al.* [2016] give flow configurations $0 < Re_* < 240$. The heat flux is constant but the buoyancy forcing is switched off for two cases which give a buoyancy to shear set-up ranging from $0 < Ri < \infty$ with our main emphasis being for $3 \cdot 10^{-3} < Ri < 5 \cdot 10^{-2}$.

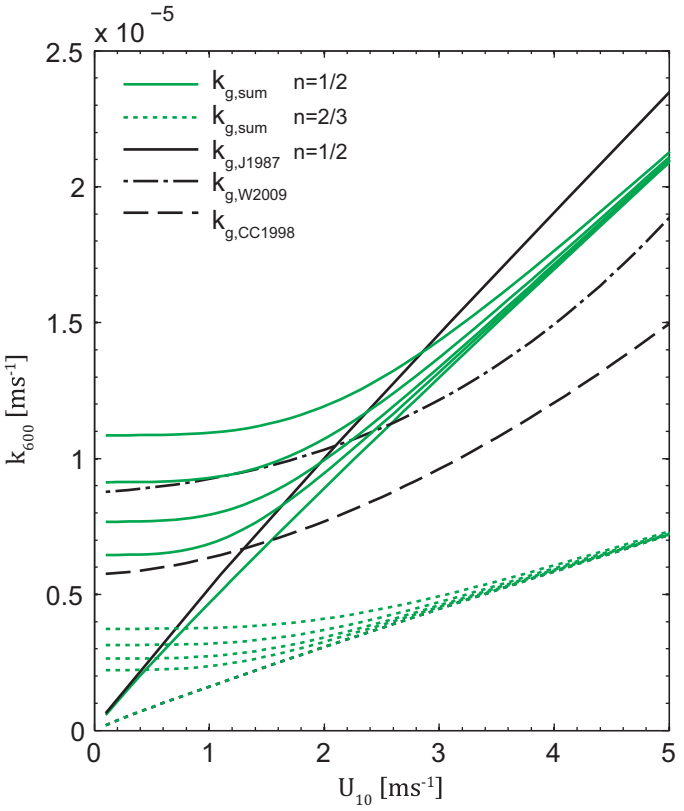


**Figure 10.** Transfer velocity $k_{g,sum}$ referenced to $Sc=600$ for $Q_0=$ 0, 50, 100, 200, and 400 $Wm^{-2}$. Full line is for $n=1/2$ and dotted is for $n=2/3$. Dashed and dash dotted lines are for the parameterizations based on wind [*Cole and Caraco*, 1998; *Wanninkhof et al.*, 2009]. $k_{g,W2009}$ is referenced from a $Sc=660$ to $Sc=600$ using equation (4) and $n=1/2$ whereas $k_{CC1998}$ is expressed for $Sc=600$ in original.

The temperature visualizations for the cases with pure shear forcing show the typical elongated streaks of warm and cold water with a streak spacing on the order of $100\nu/u_*$. The cases driven by both convection and shear show a more intriguing pattern, since when shear is "added" to the case with convection only, it is shown that the flow structures start to be elongated in the shear direction. By increasing the shear further, the surface-temperature field shows more similarity with the pure shear driven case and eventually the flow structures (surface-temperature field) have similar appearance regardless of the buoyancy forcing.

The averaged statistics for all the quantities studied (i.e., RMS velocity and vorticity, mean temperature and scalar concentration, surface flow divergence, and dissipation) indicate a transition from natural-convection (buoyancy) to shear-dominated flow at $Ri \approx 4 \cdot 10^{-3}$, which implies $U_{10}$ approximately 3 $ms^{-1}$ for natural conditions.

A parameterization of the gas transfer velocity using dissipation shows an unfavorable $Ri$ dependence for combined driven flow cases whereas the parameterizations using divergence and heat flux show smaller $Ri$ dependencies. This indicates that the dissipation rate near the surface is not as tightly connected to the gas transfer as theoretically predicted. That parameterization should therefore be used with caution. The two evaluated empirical parameterizations using wind speed give reasonable estimates of the transfer-velocity, depending however on the surface heat-flux. One such parameterization [*Wanninkhof et al.*, 2009] corresponds to a heat flux of approximately 200 $Wm^{-2}$ and the other [*Cole and Caraco*, 1998] corresponds to a heat flux of approximately 35 $Wm^{-2}$.

Furthermore, the gas-transfer is shown to be well represented by two different approaches. Both approaches use an assumption of a constant $A_{Shear}$ for both clean and contaminated surfaces. The first originates from the dissipation parameterization and sums the two dissipation scales for buoyancy and shear-driven flows which results in $k_{g,sum}=A_{Shear}u_*(Ri/Ri_c+1)^{1/4}Sc^{-n}$, whereas the second approach uses the hypothesis that there is a transition from buoyancy-driven to shear-driven gas flux. Here the transfer velocity can either be modeled with a continuous error-function or a piecewise linear function. The parameterization based on the error-function is given by $k_{g,erf}=\left[A_{Buoy}(B\nu)^{1/4}erf\left(\frac{Ri}{Ri_{c,erf}}\right)+A_{Shear}u_*erfc\left(\frac{Ri}{Ri_{c,erf}}\right)\right]Sc^{-n}$ where $Ri_{c,erf}=0.01$. The piecewise linear function express the transfer velocity due to buoyancy forcing as

$k_{g,tres}=A_{Buoy}(B\nu)^{1/4}Sc^{-n}$, down to a critical $Ri_c \approx 4\times10^{-3}$ whereafter the transfer velocity due to shear-stress, $k_{g,tres}=A_{Shear}u_*Sc^{-n}$, is used. $k_{g,sum}$ overestimates the gas flux while $k_{g,erf}$ and $k_{g,tres}$ underestimate the gas flux to some extent. $k_{g,erf}$ has a maximum error of approximately 20% while the other two have errors

of less than 10%. All these three parameterization models use critical Richardson numbers. This number can also be seen to express the transition point where the gas-flux forcing is dominated by either buoyancy flux or shear-stress.

**Acknowledgements**
The computations were performed on resources provided by the Swedish National Infrastructure for Computing (SNIC) at C3SE (Chalmers Centre for Computational Science and Engineering) computing resources. Lars Arneborg was supported by the Swedish Research Council through a grant to David Bastviken. The authors would also like to express their gratitude to the three anonymous reviewers whose input has improved the paper. The open source code for the general computational fluid dynamics model used in this study, the OpenFOAM 2.1.x, is freely available at http://www.openfoam.org/archive/2.1.0/download/git.php. The adaption source code and the input files necessary to reproduce the present DNS with OpenFOAM, are available from the authors upon request (sam.fredriksson@gu.se).

## References

Bade, D. L. (2009), Gas exchange at the air–water interface, in *Encyclopedia of Inland Waters*, edited by G. E. Likens, pp. 70–78, Academic, Oxford, U. K., doi:10.1016/B978-012370626-3.00213-1.

Banerjee, S., D. Lakehal, and M. Fulgosi (2004), Surface divergence models for scalar exchange between turbulent streams, *Int. J. Multiphase Flow*, *30*(7-8), 963–977, doi:10.1016/j.imultiphase.2004.05.004.

Broecker, W. S., and T. H. Peng (1974), Gas exchange rates between air and sea1, *Tellus*, *26*(1-2), 21–35, doi:10.1111/j.2153-3490.1974.tb01948.x.

Calmet, I., and J. Magnaudet (1998), High-Schmidt number mass transfer through turbulent gas-liquid interfaces, *Int. J. Heat Fluid Flow*, *19*(5), 522–532, doi:10.1016/S0142-727x(98)10017-6.

Ciais, P., et al. (2013), Carbon and other biogeochemical cycles, in *Climate Change 2013: The Physical Science Basis, Contribution of Working Group I to the Fifth Assessment Report of the Intergovernmental Panel on Climate Change*, edited by T.F. Stocker, et al. 1535 pp., Cambridge University Press, Cambridge, U. K., N. Y.

Cole, J. J., and N. F. Caraco (1998), Atmospheric exchange of carbon dioxide in a low-wind oligotrophic lake measured by the addition of SF6, *Limnol. Oceanogr.*, *43*(4), 647–656.

Cole, J. J., et al. (2007), Plumbing the global carbon cycle: Integrating inland waters into the terrestrial carbon budget, *Ecosystems*, *10*(1), 171–184, doi:10.1007/s10021-006-9013-8.

Csanady, G. T. (2001), *Air-Sea Interaction: Laws and Mechanisms*, vol. vii, 239 p., Cambridge Univ. Press, Cambridge, U. K.

Don, W. G., and H. P. Robert (2008), Transport properties, in *Perry's Chemical Engineers' Handbook*, 8th ed., edited by B. E. Poling et al., pp. 1–517. McGraw-Hill, N. Y.

Fairall, C. W., E. F. Bradley, J. S. Godfrey, G. A. Wick, J. B. Edson, and G. S. Young (1996), Cool-skin and warm-layer effects on sea surface temperature, *J. Geophys. Res.*, *101*(C1), 1295–1308, doi:10.1029/95JC03190.

Fredriksson, S. T., L. Arneborg, H. Nilsson, Q. Zhang, and R. A. Handler (2016), An evaluation of gas transfer velocity parameterizations during natural convection using DNS, *J. Geophys. Res. Oceans*, *121*, 1400–1423, doi:10.1002/2015JC011112.

Gålfalk, M., D. Bastviken, S. Fredriksson, and L. Arneborg (2013), Determination of the piston velocity for water-air interfaces using flux chambers, acoustic Doppler velocimetry, and IR imaging of the water surface, *J. Geophys. Res. Biogeosci.*, *118*, 770–782,10.1002/jgrg.20064.

Garbe, C. S. (2001), *Measuring Heat Exchange Processes at the Air-Water Interface from Thermographic Image Sequence Analysis*, 232 pp., Rupertus Carola Univ. of Heidelberg, Heidelberg, Germany.

Grötzbach, G. (2013), Challenges in low-Prandtl number heat transfer simulation and modelling, *Nucl. Eng. Design*, *264*, 41–55, doi:10.1016/j.nucengdes.2012.09.039.

Handler, R. A., and Q. Zhang (2013), Direct numerical simulations of a sheared interface at low wind speeds with applications to infrared remote sensing, *IEEE J-Stars*, *6*(3), 1086–1091, doi:10.1109/Jstars.2013.2241736.

Handler, R. A., G. B. Smith, and R. I. Leighton (2001), The thermal structure of an air-water interface at low wind speeds, *Tellus, Ser. A*, *53*(2), 233–244.

Hasegawa, Y., and N. Kasagi (2008), Systematic analysis of high Schmidt number turbulent mass transfer across clean, contaminated and solid interfaces, *Int. J. Heat Fluid Flow*, *29*(3), 765–773, doi:10.1016/j.ijheatfluidflow.2008.03.002.

Herlina, H., and J. G. Wissink (2014), Direct numerical simulation of turbulent scalar transport across a flat surface, *J. Fluid Mech.*, *744*, 217–249, doi:10.1017/jfm.2014.68.

Jahne, B., and H. Haussecker (1998), Air-water gas exchange, *Annu. Rev. Fluid Mech.*, *30*, 443–468.

Jahne, B., K. O. Munnich, R. Bosinger, A. Dutzi, W. Huber, and P. Libner (1987), On the parameters influencing air-water gas-exchange, *J. Geophys. Res.*, *92*(C2), 1937–1949.

Jerlov, N. G. (1976), *Marine Optics*, Elsevier Sci., Elsevier, Amsterdam.

Kim, J., and P. Moin (1989), Transport of passive scalars in a turbulent channel flow, in *Turbulent Shear Flows*, vol.6, edited by J.-C. André et al., pp. 85–96, Springer, Berlin, doi:10.1007/978-3-642-73948-4_9.

Kim, J., P. Moin, and R. Moser (1987), turbulence statistics in fully-developed channel flow at low Reynolds-number, *J. Fluid Mech.*, *177*, 133–166, doi:10.1017/S0022112087000892.

Kubrak, B., H. Herlina, F. Greve, and J. G. Wissink (2013), Low-diffusivity scalar transport using a WENO scheme and dual meshing, *J. Comput. Phys.*, *240*, 158–173, doi:10.1016/j.jcp.2012.12.039.

Kundu, P. K., I. M. Cohen, and D. R. Dowling (2012), *Fluid Mechanics*, 5th ed., Elsevier, Oxford, U. K.

Ledwell, J. J. (1984), The variation of the gas transfer coefficient with molecular diffusivity, in *Gas Transfer at Water Surfaces*, edited by W. Brutsaert and G. H. Jirka, pp. 293–302, Dordrecht, Reidel.

Leighton, R. I., G. B. Smith, and R. A. Handler (2003), Direct numerical simulations of free convection beneath an air-water interface at low Rayleigh numbers, *Phys. Fluids*, *15*(10), 3181–3193, doi:10.1063/1.1606679.

Magnaudet, J., and I. Calmet (2006), Turbulent mass transfer through a flat shear-free surface, *J Fluid Mech.*, *553*, 155–185, doi:10.1017/S0022112006008913.

Na, Y., D. V. Papavassiliou, and T. J. Hanratty (1999), Use of direct numerical simulation to study the effect of Prandtl number on temperature fields, *Int. J. Heat Fluid Flow*, *20*(3), 187–195, doi:10.1016/S0142-727x(99)00008-9.

Nagaosa, R., and R. A. Handler (2012), Characteristic time scales for predicting the scalar flux at a free surface in turbulent open-channel flows, *AIChE J.*, *58*(12), 3867–3877, doi:10.1002/aic.13773.

Nagaosa, R. S. (2014), Reprint of: A numerical modelling of gas exchange mechanisms between air and turbulent water with an aquarium chemical reaction, *J. Comput. Phys.*, *271*, 172–190, doi:10.1016/j.jcp.2014.04.007.

Rantakari, M., J. Heiskanen, I. Mammarella, T. Tulonen, J. Linnaluoma, P. Kankaala, and A. Ojala (2015), Different apparent gas exchange coefficients for CO2 and CH4: Comparing a brown-water and a clear-water lake in the boreal zone during the whole growing season, *Environ. Sci. Technol.*, *49*(19), 11,388–11,394, doi:10.1021/acs.est.5b01261.

Rutgersson, A., and A. Smedman (2010), Enhanced air-sea CO2 transfer due to water-side convection, *J. Mar. Syst.*, *80*(1-2), 125–134, doi:10.1016/j.jmarsys.2009.11.004.

Soloviev, A. X., and P. Schlussel (1994), Parameterization of the cool skin of the ocean and of the air ocean gas transfer on the basis of modeling surface renewal, *J. Phys. Oceanogr.*, *24*(6), 1339–1346

Wanninkhof, R., W. E. Asher, D. T. Ho, C. Sweeney, and W. R. McGillis (2009), Advances in quantifying air-sea gas exchange and environmental forcing, *Annu. Rev. Mar. Sci.*, *1*, 213–244, doi:10.1146/annurev.marine.010908.163742.

Wissink, J. G., and H. Herlina (2016), Direct numerical simulation of gas transfer across the air–water interface driven by buoyant convection, *J. Fluid Mech.*, *787*, 508–540, doi:10.1017/jfm.2015.696.

Zhang, Q., R. A. Handler, and S. T. Fredriksson (2013), Direct numerical simulation of turbulent free convection in the presence of a surfactant, *Int. J. Heat Mass Transfer*, *61*, 82–93, doi:10.1016/j.ijheatmasstransfer.2013.01.031.